Dalton
Transactions

Thermal atomic layer deposition of Er2O3 films from a volatile, thermally stable enaminolate precursor

Journal:	*Dalton Transactions*
Manuscript ID	DT-ART-06-2023-001824.R1
Article Type:	Paper
Date Submitted by the Author:	12-Jul-2023

Complete List of Authors:	Jayakodiarachci, Navoda; Wayne State University, Department of Chemistry Liu, Rui; University of Wisconsin-Madison, Department of Materials Science and Engineering Dharmadasa, Chamod; Wayne State University, Department of Chemistry Hu, Xiaobing; Northwestern University, Department of Materials Science and Engineering Savage, Don; University of Wisconsin-Madison, Material Science and Engineering and Physics Ward, Cassandra; Wayne State University Evans, Paul; University of Wisconsin-Madison, Department of Materials Science and Engineering Winter, Charles; Wayne State University, Department of Chemistry

SCHOLARONE™
Manuscripts

ARTICLE

Thermal atomic layer deposition of Er_2O_3 films from a volatile, thermally stable enaminolate precursor

Navoda Jayakodiarachchi,[a] Rui Liu,[b] Chamod Dharmadasa,[a] Xiaobing Hu,[c] Donald E. Savage,[b] Cassandra L. Ward,[a] Paul G. Evans,[b] and Charles H. Winter*[a]

Received 00th January 20xx,
Accepted 00th January 20xx

DOI: 10.1039/x0xx00000x

Thin films of Er_2O_3 films were grown by atomic layer deposition using the Er precursor tris(1-(dimethylamino)-3,3-dimethylbut-1-en-2-olate)erbium(III) ($Er(L^1)_3$), with water as the co-reactant. Saturative, self-limited growth was observed at a substrate temperature of 200 °C for pulse lengths of ≥4.0 s for $Er(L^1)_3$ and ≥0.2 s for water. An ALD window was observed from 175 to 225 °C with a growth rate of about 0.25 Å/cycle. Er_2O_3 films grown at 200 °C on Si(100) and SiO_2 substrates with a thickness of 33 nm had root mean square surface roughnesses of 1.75 and 0.75 nm, respectively. Grazing incidence X-ray diffraction patterns showed that the films were composed of polycrystalline Er_2O_3 at all deposition temperatures on Si(100) and SiO_2 substrates. X-ray photoelectron spectroscopy revealed stoichiometric Er_2O_3, with carbon and nitrogen levels below the detection limits after argon ion sputtering to remove surface impurities. Transmission electron microscopy studies of Er_2O_3 film growth in nanoscale trenches (aspect ratio = 10) demonstrated conformal coverage.

Introduction

Lanthanide oxide-containing thin films have numerous applications, including as high dielectric constant (κ) materials for microelectronics, in producing two-dimensional electron gases on substrates such as TiO_2-terminated $SrTiO_3$, as luminescent materials, optical coatings, superconductors, and catalytic materials.[1-8] Among the lanthanide oxides, Er_2O_3 has attracted attention because of its high dielectric constant (κ ~14),[9] large bandgap (~7 eV),[10] conduction band offset on Si (~3.5 eV),[11,12] thermodynamic stability at high temperatures,[13] high refractive index (~1.6-1.7),[14] transparency in the UV and visible range,[15] and limited hydroxylation owing to the smaller ionic radius of Er^{3+} ion relative to the earlier lanthanide(III) ions.[16] Because of these properties, Er_2O_3 films have been investigated as high κ materials in complementary metal oxide semiconductor (CMOS) devices, antireflection coatings in solar cells, protective coatings, and passivation layers for III-V semiconductors.[12,17-21] Additionally, the Er^{3+} ion has been extensively used in telecommunications technologies because of its 1550 cm^{-1} emission that corresponds to a low absorption window of silica optical fibers.[22,23]

Deposition of Er_2O_3 films has been achieved using several chemical and physical vapor deposition techniques, such as molecular beam epitaxy (MBE),[18,19] reactive evaporation,[21] electron beam evaporation,[23] sputtering,[14,23,24] sol-gel methods,[25] pulsed laser deposition,[26] metalorganic chemical vapor deposition,[10,27-29] and atomic layer deposition (ALD).[30-48] Among these techniques, ALD has the unique advantages of Angstrom-level thickness control, perfect conformal coverage at the nanoscale in high aspect ratio features, and film growth at low to moderate temperatures.[49,50] In spite of the attractive features of Er_2O_3 ALD growth, the range of ALD studies for Er_2O_3 films is limited. Er_2O_3 ALD processes have predominantly used $Er(thd)_3$[30-36] (thd = 2,2,6,6-tetramethylheptane-3,5-dionate) and Er cyclopentadienyl precursors.[37-45] With $Er(thd)_3$, thermal ALD processes require ozone as the co-reactant, since water does not react.[30,31] Plasma-based processes with $Er(thd)_3$ have employed O_2 plasma as the co-reactant.[32-36] Cyclopentadienyl-based precursors have included $Er(C_5H_4Me)_3$, $Er(C_5H_4nBu)_3$, $Er(C_5H_4iPr)_3$, or $Er(C_5H_4Me)_2(iPrNC(Me)NiPr)$ in thermal ALD processes with water or ozone as the co-reactant and O_2 plasma in plasma-based processes.[37-45] Several additional precursors for Er_2O_3 ALD have been reported. The ALD behavior of the Er amidinate precursor, $Er(tBuNC(Me)NtBu)_3$, was explored using water and ozone as co-reactants.[46] $Er(tBuNC(Me)NtBu)_3$ was unreactive towards water, but gave nearly stoichiometric films with low impurity levels using ozone as the co-reactant. The related guanidinate precursor, $Er(iPrNC(NMe_2)NiPr)_3$, was used for the ALD of Er_2O_3 films with water as the co-reactant.[47,48]

A significant challenge in designing ALD precursors for the growth of Er_2O_3 films is the ability to use water as a co-reactant, since ozone and O_2 plasma can oxidize the surfaces of sensitive substrates such as silicon and many metals. The pK_a values for ligands can be used to predict the favorability of ligand protonations by water (pK_a = 14.0 or 15.7)[51] and can thus be useful tools for designing new ALD precursors, although other

[a.] Department of Chemistry, Wayne State University, Detroit, Michigan 48202 USA.
[b.] Department of Materials Science and Engineering, University of Wisconsin-Madison, Madison, Wisconsin 53706 USA.
[c.] Department of Materials Science and Engineering and Atomic and Nanoscale Characterization Experimental Center, Northwestern University, Evanston, Illinois 60208, USA.
† Footnotes relating to the title and/or authors should appear here.
Electronic Supplementary Information (ESI) available: [details of any supplementary information available should be included here]. See DOI: 10.1039/x0xx00000x

factors such as bond energy changes during reactions are also important. For example, 2,4-pentanedione (pK_a = 9[52]) has a lower pK_a value than that of water, indicating that protonation of 2,4-pentanedionate by water is unfavorable. The unfavorable protonation reaction predicted by pK_a values reflects the lack of reactivity of the β-diketonate precursor $Er(thd)_3$ with water in attempted Er_2O_3 ALD growth.[30,31] While erbium precursors containing cyclopentadienyl ligands react with water in ALD processes,[37] the pK_a value of cyclopentadiene (pK_a = 16[52]) is only slightly more positive than that of water, suggesting only a moderate driving force for protonation.

We recently reported the syntheses, structural characteristics, volatilities, and thermal stabilities of lanthanide(III) complexes containing enaminolate ligands that are derived from deprotonation of α-amino ketones.[53] Herein, we report the optimization of the ALD growth of Er_2O_3 films using the enaminolate precursor, tris(1-(dimethylamino)-3,3-dimethylbut-1-en-2-olate)erbium(III) (**1**, Fig. 1), with water as the co-reactant. Importantly, the pK_a value of the α-amino ketone $PhC(=O)CH_2NMe_2$ is 23.55,[54] which ensures a strongly favorable protonolysis reaction during ALD using **1** with water as the co-reactant. The Er_2O_3 films were characterized to assess thickness trends, structure, morphology, and composition using scanning electron microscopy (SEM), grazing incidence X-ray diffraction (GI-XRD), atomic force microscopy (AFM), and X-ray photoelectron spectroscopy (XPS). Additionally, films were deposited in high aspect ratio trenched substrates. Cross-sectional transmission electron microscopy (TEM) was used to determine the conformal coverage and to demonstrate that this process forms continuous films at low Er_2O_3 thicknesses.

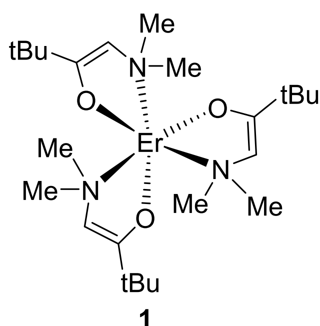

Fig. 1 Chemical structure of precursor **1**.

Experimental

ALD experiments were performed using a Picosun R-75BE ALD reactor at substrate temperatures of 150-275 °C. An Alcatel 2063 C2 oil pump with a pumping speed of 56 m^3/h was used to provide vacuum. Depositions were carried out on thermal SiO_2 (thickness ~300 nm) on Si and Si(100) with native oxide (~2 nm) substrates. Additional depositions were carried out on Cu/TiN (~60 nm)/SiO_2 (~100 nm)/Si, Ru (~16 nm)/SiO_2, TiN, Pt (~10 nm)/SiO_2, W, single-crystal $SrTiO_3$ (STO), and single crystal sapphire (α-Al_2O_3) substrates. Depositions on all of the substrates except on STO and sapphire were carried out without prior cleaning. STO and sapphire substrates were subjected to cleaning procedures reported in the literature.[55,56] The ALD reactor intermediate chamber pressure was maintained at 3-8 Torr during the depositions and ultra-high purity nitrogen (99.999%, Airgas) was used as both the carrier and purge gas. Nitrogen gas flows of 80 sccm through the source lines into the chamber and 150 sccm to the intermediate space were employed. Erbium precursor **1** was synthesized following the previously reported procedure and was sublimed prior to use.[53] Precursor **1** was delivered using a Picosolid booster at 125 °C and water was delivered using a conventional vapor draw bubbler at 23 °C.

Film thicknesses were measured using spectroscopic ellipsometry (J. A. Woollam Co. Alpha-SE) with a wavelength of 632.8 nm and an incident angle of 65° and were confirmed by cross-sectional SEM (JEOL-6510LV) and X-ray reflectivity (XRR). XRR measurements were performed using a PANalytical Empyrean X-ray diffractometer with CuKα radiation. The crystallinity of the films was evaluated by GI-XRD using a Bruker D8 Advance diffractometer with Cu Kα radiation at 1.54 Å wavelength and an incident angle of ω = 0.5° with a detector (2θ) scan range of 5-68°. The surface morphology was explored using a Bruker Icon AFM operated in a non-contact imaging mode. XPS analyses were carried out to determine the film composition using a NEXSA ThermoFisher Scientific spectrometer, equipped with a monochromatic Al Kα (1486.7 eV) X-ray source operating at 12 kV and 6 mA. The electron transparent lamella sample for the TEM analysis was prepared using a Helios Nanolab. All TEM observations were conducted on ARM 200CF, which was operated at 200 kV. This microscope was equipped with a probe corrector and dual silicon drift detectors. For a single detector, the area is 100 mm^2 and overall solid angle of this energy dispersive spectrum (EDS) system is around 1.8 sr. The convergence angle in scanning transmission electron microscopy (STEM) mode was 28 mrad and collection angle of bright field imaging was 0-22 mrad.

Results and discussion

Precursor Selection and Initial Studies

The synthesis, characterization, volatility, and thermal stability of **1** were described in our recent report.[53] Precursor **1** has a melting point of 93-95 °C, a distillation temperature of ~110 °C at 0.5 Torr, and a decomposition temperature of ~265 °C. Since **1** has a melting point below its delivery temperature in the ALD reactor, vapor transport occurs from the liquid state. Liquid precursors are advantageous for use in ALD, since the surface areas of liquids are approximately constant and thus afford constant concentrations of precursors in the gas phase. The surface areas of solid precursors may change under vapor transport conditions, leading to changing gas phase concentrations with precursor loading. Complex **1** exhibits a single-step weight loss in the thermogravimetric analysis up to about 240 °C, at which point decomposition appears to ensue.[53] These thermal and physical precursor properties are very promising and **1** was thus chosen for evaluation in Er_2O_3 ALD. The X-ray crystal structure of **1** was not described in our original report, but was obtained during this work. Complex **1** adopts a monomeric, 6-

This journal is © The Royal Society of Chemistry 2023

Please do not adjust margins

coordinate distorted octahedral geometry, with structural features very similar to those of the Lu analog.[53] The structural data of **1** are presented in the ESI (Tables S1-S3, Fig. S1).

Self-limited growth

To probe the self-limited growth behavior and obtain the optimum saturative pulse length for each precursor, ALD experiments were carried out at a substrate temperature of 200 °C with 1000 ALD cycles on Si(100) and SiO_2 substrates. The saturative growth behavior of **1** was evaluated first using the following pulse/purge sequence: **1** (varied), N_2 purge (8.0 s), water (0.3 s), and N_2 purge (10.0 s). As depicted in Fig. 2, saturative growth was observed for pulse durations longer than 4.0 s for **1** with a growth rate of 0.25 Å/cycle. The origin of the similar growth rates (~0.14 Å/cycle) for **1** at pulse lengths of 1 and 2 s is unclear and will require further experimentation. The self-limited growth behavior of the water precursor was evaluated next. A pulse/purge sequence of **1** (5.0 s), N_2 purge (8.0 s), water (varied), and N_2 purge (10.0 s) was used for 1000 ALD cycles at 200 °C. As depicted in Fig. 3, the growth rate was constant for water pulse lengths longer than 0.2 s with a saturative growth rate of 0.25 Å/cycle. The process employing **1** and water thus clearly exhibits self-limited growth at 200 °C.

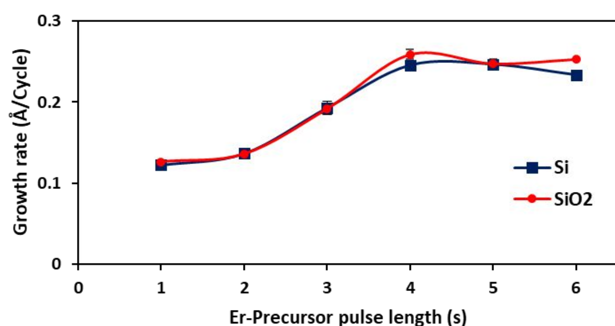

Fig. 2 Dependence of Er_2O_3 film growth rate on the pulse length of **1**. Si(100) and SiO_2 substrates were used at 200 °C with 1000 growth cycles.

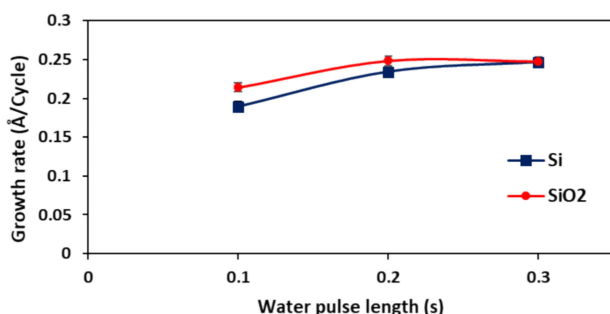

Fig. 3 Dependence of Er_2O_3 film growth rate on the water pulse length. Si(100) and SiO_2 substrates were used at 200 °C with 1000 growth cycles.

Substrate temperature dependence

To assess the dependence of the Er_2O_3 growth rate on the deposition temperatures, ALD experiments were carried out in the substrate temperature range of 150 to 275 °C, with 25 °C temperature increments. Depositions were conducted with the optimized precursor pulse and purge lengths established above: **1** (5.0 s)/N_2 purge (8.0 s)/water (0.2 s)/N_2 purge (10.0 s)) with 1000 ALD cycles. As illustrated in Fig. 4, the growth rate increased from 0.20 Å/cycle at 150 °C to 0.25 Å/cycle at 175 °C and a constant growth rate of about 0.25 Å/cycle was maintained in the temperature range of 175 to 225 °C. The temperature range with a constant growth rate represents the ALD window for this process.[49,50] The lower growth rate observed at 150 °C is likely due to insufficient thermal energy to drive the surface reactions. At 250 and 275 °C, the growth rate decreased from 0.25 Å/cycle to about 0.15 Å/cycle. These lower growth rates could either be due to thermal decomposition before the precursor reaches the substrate surface, as evidenced by decomposition of precursor **1** at 265 °C,[53] or because of dehydration of surface Er-OH groups above 250 °C, resulting in fewer surface reactive sites.

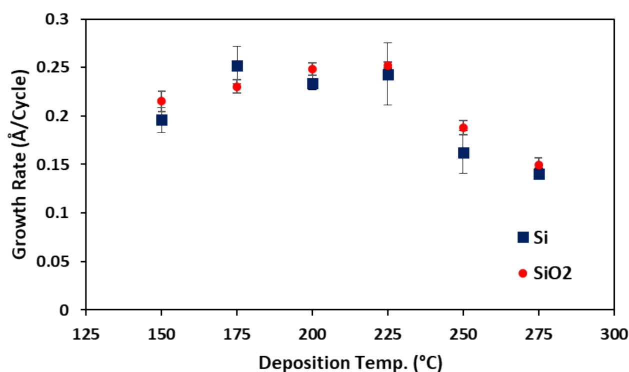

Fig. 4 Dependence of Er_2O_3 film growth rate on Si(100) and SiO_2 substrates as a function of deposition temperature.

Dependence of film thickness on the number of growth cycles

The relationship between film thickness and the number of ALD cycles was examined by depositing Er_2O_3 layers at a substrate temperature of 200 °C using the optimized precursor pulse and purge lengths outlined above. As shown in Fig. 5 for films grown on Si(100) substrates, the film thicknesses were proportional to the number of ALD cycles. Identical behavior was observed for films grown on thermal SiO_2 substrates (Fig. S2). The slopes of the plots gave growth rates of 0.31 and 0.29 Å/cycle on Si(100) and SiO_2 substrates, respectively. The best fit lines did not pass through the origins, indicating that there were nucleation delays before the depositions reach the steady-state growth rates. For both substrates, the nucleation delays were about 200 cycles, based upon the best-fit lines. Because of the nucleation delays, the growth rate of ~0.25 Å/cycle shown in Figs. 1-3 is slightly smaller than the values derived from Fig. 4. The growth rate of 0.30 Å/cycle observed in this work is similar to the growth rate of an $Er(thd)_3/O_3$ ALD process (0.25 Å/cycle),[30] but is lower than other previous Er_2O_3 ALD processes

Please do not adjust margins

($Er(C_5H_4Me)_3/H_2O$ ~1.5 Å/cycle,[37] $Er(tBuNC(Me)NtBu)_3/O_3$ ~0.51 Å/cycle,[46] $Er(iPrNC(NMe_2)NiPr)_3/H_2O$ ~1.1 Å/cycle[47]). However, the high reactivity of **1** toward water is advantageous compared to the $Er(thd)_3$ and $Er(tBuNC(Me)NtBu)_3$ precursors that required ozone for Er_2O_3 film growth.[30,46]

Fig 5 Dependence of Er_2O_3 film thicknesses on the number of ALD cycles with a Si(100) substrate at 200 °C.

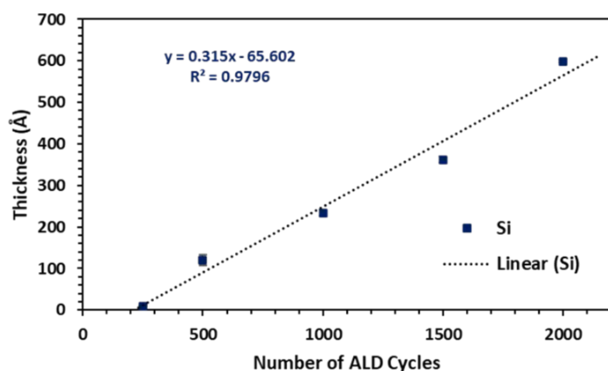

Structure and morphology

The surface roughness and other properties of the surface morphology were probed by using AFM to characterize 33 nm thick Er_2O_3 films deposited at a substrate temperature of 200 °C on Si(100) and SiO_2 substrates. The root mean square (RMS) roughness values over 1 μm² x 1 μm² areas on Si(100) and SiO_2 substrates were 1.76 and 0.75 nm, respectively (Fig. 6).

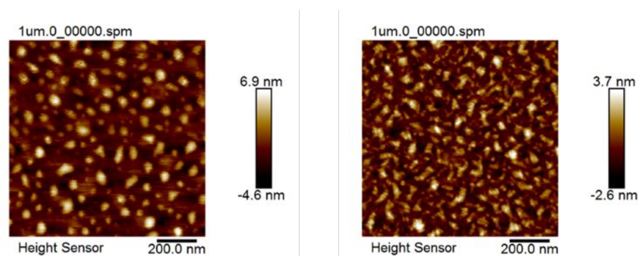

Fig. 6 AFM height images of 33 nm thick Er_2O_3 thin films grown on Si(100) (left, RMS roughness = 1.76 nm) and SiO_2 (right, RMS roughness = 0.75 nm) at a substrate temperature of 200 °C.

The crystallinity of the as-deposited Er_2O_3 films was studied with ~25 nm thick Er_2O_3 films grown at substrate temperatures of 150, 200, and 250 °C on Si(100) and SiO_2 with 1000 ALD cycles. Fig. 7 shows the GI-XRD diffraction patterns of films grown on Si(100) substrates. Films grown on SiO_2 substrates showed very similar diffraction patterns (Fig. S3). The reflections correspond to a cubic phase of Er_2O_3. The simultaneous observation of reflections from multiple families indicates that Er_2O_3 layers are polycrystalline. The grain size within the Er_2O_3 films was larger at higher deposition temperatures, as measured using the Scherrer equation for the most intense (222) reflection. The measured crystal sizes were ~2 and ~6 nm for films deposited at substrate temperatures of 150 and 250 °C, respectively.

For further insights into film density, thickness, and roughness, XRR measurements were conducted on the same samples that were used for AFM. XRR fitting data further confirmed the Er_2O_3 film thicknesses (31.3 nm on Si(100) and 31.7 nm on SiO_2) determined using ellipsometry (33 nm on both Si(100) and SiO_2) to be accurate. The Er_2O_3 film density extracted from XRR fitting data for the film deposited on Si(100) was about 7.3 gm/cm³, while the film deposited on SiO_2 was around 7.1 gm/cm³. These density values extracted from XRR correspond to 82 to 84% of the bulk Er_2O_3 density (8.64 gm/cm³).[23] Data are presented in Fig. S4. In addition, XRR data also revealed smooth Er_2O_3 films, with 0.575 nm (1.8%) and 1.0 nm (3.2%) roughness values for the 31 nm thick Er_2O_3 films on Si and SiO_2, respectively. Plan view SEM images of films on Si(100) and SiO_2 (Fig. S5) also showed very smooth surfaces. Er_2O_3 films were also grown on Cu, Ru, TiN, Pt, and W substrates at 200 °C with 1500 ALD cycles. Fig. S6 reveals similar growth rates to the films grown on Si(100) and SiO_2, and GI-XRD demonstrated the formation of polycrystalline Er_2O_3 (Fig. S7).

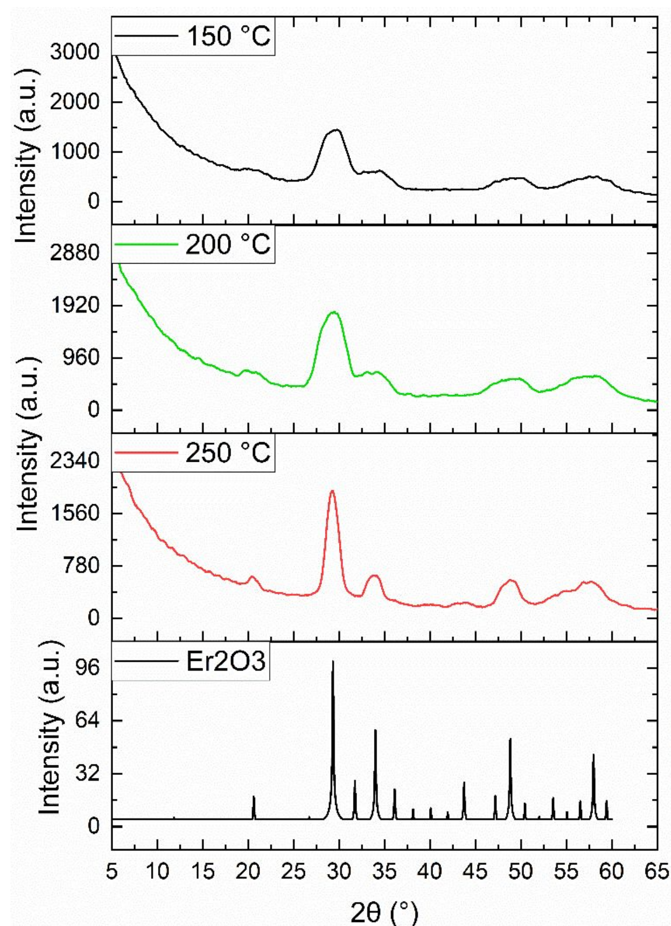

Fig. 7 X-ray diffraction patterns of 25 nm thick Er_2O_3 thin films deposited at substrate temperatures of 150, 200, and 250 °C on Si(100) with 1000 cycles. The dotted lines represent the reference for cubic Er_2O_3 (COD 1010334 Er_2O_3).

The crystallinity of the Er_2O_3 films was further investigated on single crystal $SrTiO_3$ (001) and sapphire (0001) substrates. TiO_2 termination of $SrTiO_3$ substrates (STO) was obtained through a

 This journal is © The Royal Society of Chemistry 2023

sequence of high temperature annealing, dissolution in water, and subsequent high temperature annealing, whereas C-plane sapphire substrates were annealed at 1400 °C to obtain atomically smooth surfaces. Annealing of STO and sapphire substrates prior to deposition was carried out following previously established protocols.[55,56] The TiO_2-terminated surface plays a crucial role in inducing interface phenomena such as a two-dimensional electron gas. The motivation behind this work was to investigate the possibility of epitaxial growth of Er_2O_3 films with preferred 00L or 000L orientation on these atomically smooth single-crystal STO (001) and sapphire (0001) substrates. However, as shown in Fig. S8, Er_2O_3 films deposited on both substrates were polycrystalline and did not show an epitaxial relationship with the substrates at the deposition temperature of 200 °C. The film deposited on the STO substrate exhibits a preferred orientation around the Er_2O_3 (004) reflection. The full width at half maximum of the rocking curve for this texture is 7°.

Film compositions

The elemental composition and chemical purity of the Er_2O_3 layers were studied using XPS to probe a 35 nm thick film deposited at 200 °C on a Si(100) substrate with native oxide. Fig. 8 shows the $Er4d_{5/2}$, O1s, and C1s binding energy regions for the Er_2O_3 film deposited at 200 °C. The spectral peaks were fit using a Lorentzian-Gaussian function (fitting curves are not shown). The binding energy of the C1s peak (284.5 eV) of adventitious C present before sputtering the film surface was used as the reference. The intensity of the C1s ionization at 284.5 eV shown in Fig. 8c was low, but a high resolution scan of the C1s region showed a C1s peak with better signal to noise ratio that was used as the reference (Fig. S9g).

The surface of the as-deposited Er_2O_3 film prior to Ar ion etching included Er, O, and C. The characteristic $Er4d_{5/2}$ ionization of the Er^{3+} ion in Er_2O_3 appeared at 168.1 eV (Fig. 8a). The intensity of this peak increased significantly at longer Ar ion etching times. Two peaks were observed in the O1s spectral region, as shown in Fig. 8b. The O1s ionization at 528.8 eV corresponds to the oxide ion in Er_2O_3 while the peak at the higher binding energy side (531.2 eV) can be attributed to hydroxide ion in $Er(OH)_3$. Er_2O_3 films with similar Er $4d_{5/2}$ and O1s binding energies and O1s ionization evolution upon Ar ion sputtering have been previously reported.[23,24,47,57,58] Interestingly, the O1s spectra collected after 2 minutes of Ar ion sputtering showed a drastic decrease in the intensity of the 531.2 eV peak. Reduction of this ionization upon sputtering indicates that $Er(OH)_3$ is absent in the bulk of the Er_2O_3 film. We propose that the 531.2 eV ionization corresponds to surface hydrolysis by moisture upon exposure of the film to ambient atmosphere. Surface hydrolysis is common for Ln_2O_3 films because of their hygroscopic nature.[24,57]

The disappearance of the C1s binding energy peak upon etching, Fig. 8c, indicates that C atoms of the ligands in **1** are completely removed during film growth. No N1s ionizations were observed in the bulk of the film (Fig. S9), which additionally supports efficient ligand removal. A broad ionization was observed at a binding energy of 100 eV, which appears in the Si2p ionization region (Fig. S9) and might suggest either Si contamination or incomplete coverage of the substrate. However, no Si2s peak was observed in the film (Fig. S9), implying that the possible Si2p peak is not due to the Si(100) substrate. A similarly broad XPS peak in the Si2p region was observed for Er_2O_3 films deposited using electron beam evaporation, which the authors claimed arose from the Er MVV Auger ionization rather than from Si2p.[23]

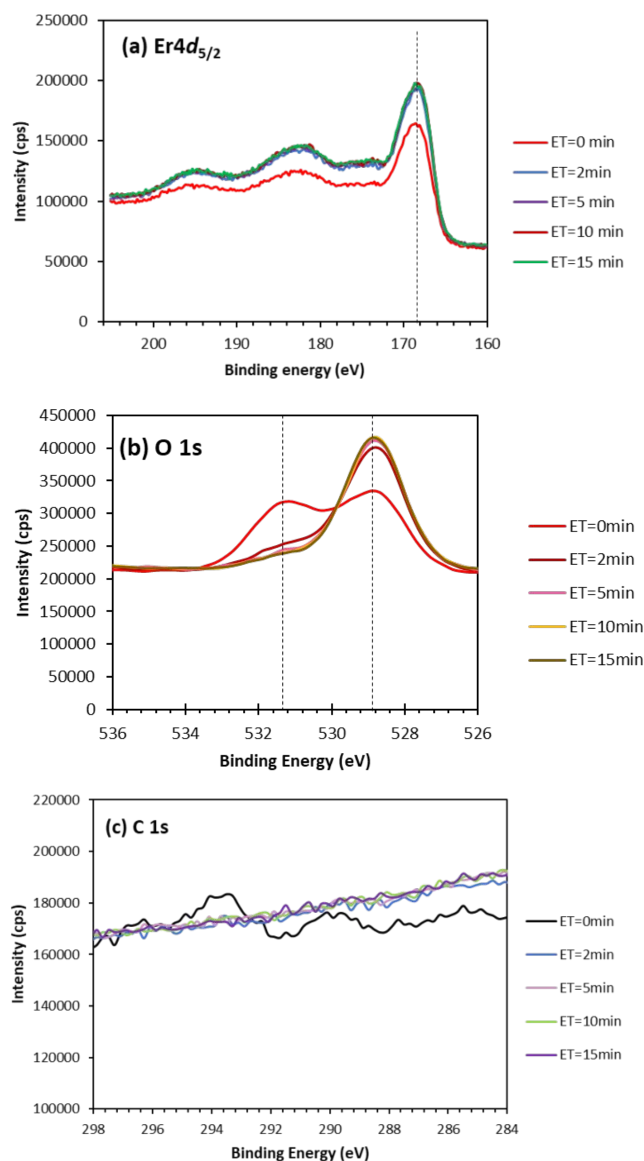

Fig. 8 High-resolution XPS spectra of $Er4d_{5/2}$ (a), O1s (b), C1s (c) of the Er_2O_3 thin film grown on a Si(100) at a substrate temperature of 200 °C with 1500 cycles at various Ar ion etching times (ETs).

Fig. 9 shows an XPS depth profile obtained for a 35 nm thick Er_2O_3 film deposited on a Si(100) substrate at 200 °C with 1000 cycles. Depth profiling was carried out by removing the surface layers using sputtering with 300 eV Ar ions. A uniform distribution of Er and O atoms throughout the film was observed and C and N contamination levels were below the detection limits. The lack of Si ionizations in the film bulk is consistent with a continuous, closed film. The average Er:O ratio was approximately 1:1.63, which is close to the atomic ratio of 1:1.5 for Er_2O_3. Fig. S9 shows Er4d and O1s binding energy scans in the bulk of the film, with peak fitting.

This journal is © The Royal Society of Chemistry 2023

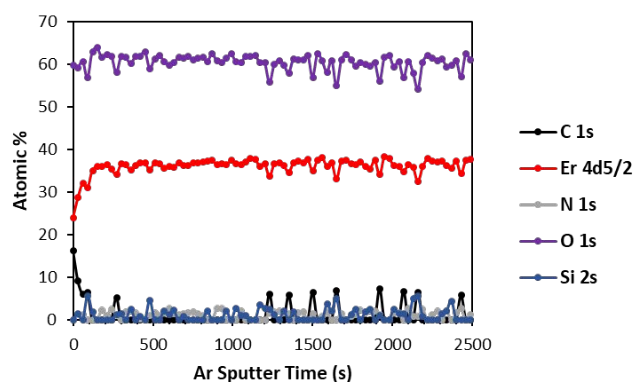

Fig. 9 XPS depth profile of a 35 nm thick Er_2O_3 thin film grown on a Si(100) substrate at 200 °C.

Conformality of deposition in high aspect ratio features

The conformality of the growth of Er_2O_3 films was explored in trenched SiO_2 substrates with aspect ratios of 10, with a width of about 30 nm at half height and a depth of about 300 nm. The deposition was conducted at a substrate temperature of 200 °C for 380 cycles using the optimized pulse and purge sequence described above. This process was predicted to afford a 10 to 11 nm thick Er_2O_3 layer, based upon the previously observed growth rates of 0.25 to 0.30 Å/cycle. TEM was used to study the conformality of the film inside the high aspect ratio trenches. The BF-STEM image and associated EDS maps shown in Fig. 10 illustrated the conformal coverage of Er_2O_3 thin films within the high aspect ratio trenches. In order to keep the intrinsic features of the trenches, carbon and platinum layers were deposited on the surface of device during the sample preparation process. Therefore, the areas in between the trenches were filled with carbon and some diffused platinum. Upon ion milling, carbon is preferably removed, which leads to the light contrast within the trenches. The top surface of each trench is also free of Er_2O_3, considering that the platinum layer is still intact as shown in Fig. 10d. The origin of this effect is not known. Based on images shown in Fig. 10, the average thickness of the Er_2O_3 layers is around 12 nm with a standard deviation of 2 nm (Table S4, Fig. S11). This measurement agrees well with our predicted film thickness described above.

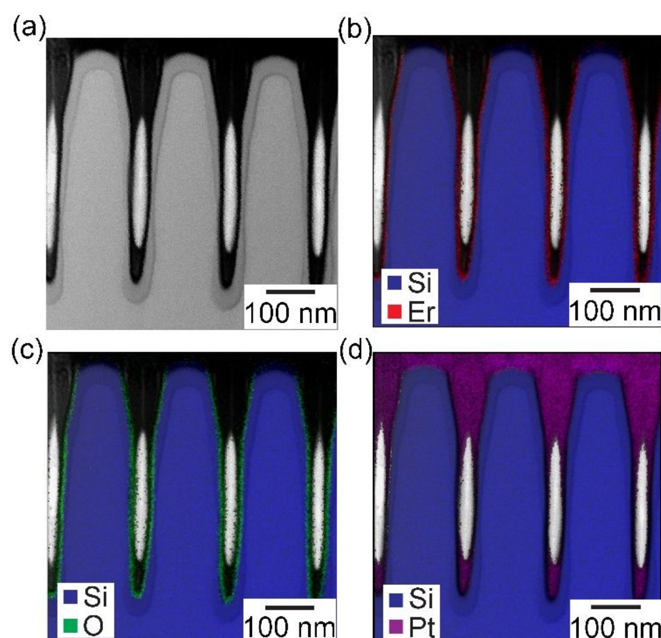

Fig. 10 Microstructural and element characterization of an Er_2O_3 film on a trenched substrate: (a) BF-STEM image displaying the trenched structure, (b) Overlapped EDS map of Er and Si elements, (c) Overlapped EDS map of O and Si elements, (d) Overlapped EDS map of Pt and Si elements.

Conclusions

Herein, we have demonstrated the growth of Er_2O_3 films by thermal ALD using the erbium enaminolate precursor **1** with water as the co-reactant. Self-limited growth was established for both **1** and water at a substrate temperature of 200 °C, with a growth rate of about 0.25 Å/cycle within the ALD window of 175-225 °C. There was a nucleation delay of about 200 cycles on Si(100) and SiO_2 substrates, after which the thickness increased linearly with increasing number of cycles. A growth rate of 0.30 Å/cycle ensued after the nucleation delay. The as-deposited Er_2O_3 films were polycrystalline on all substrates, and AFM, XRR, and SEM revealed smooth surfaces. XPS analyses of a film grown at 200 °C showed stoichiometric Er_2O_3 with C and N levels below the detection limits in the film bulk. TEM studies of Er_2O_3 films deposited in trenched substrates with aspect ratios of about 10 afforded perfect conformal coverage of the trenches. The successful growth of Er_2O_3 films from **1** and water suggests that our other recently reported La, Pr, Nd, Y, and Lu enaminolate complexes[53] should also serve as Ln_2O_3 ALD precursors with water as the co-reactant.

Conflicts of interest

There are no conflicts to declare.

Acknowledgements

This research was primarily supported by the U.S. National Science Foundation through the University of Wisconsin Materials Research Science and Engineering Center (DMR-1720415). U.S. National Science Foundation Grant Nos. CHE-1427926, ECCS-1849578, and DMR-0922912 are acknowledged for the purchase of a powder X-ray diffractometer, X-ray photoelectron spectrometer, and a field emission SEM at Wayne State University, respectively. This work also made use of a single-crystal X-ray diffractometer that was funded by the National Institutes of Health supplement grant #3R01EB027103-02S1. The authors gratefully acknowledge the use of facilities and instrumentation at the UW-Madison Wisconsin Centers for Nanoscale Technology (wcnt.wisc.edu), which is partially supported by the U.S. National Science Foundation through the University of Wisconsin Materials Research Science and Engineering Center (DMR-1720415). This work also made use of the EPIC facility of Northwestern University's NU*ANCE* Center, which has received support from the SHyNE Resource (NSF ECCS-2025633), the IIN, and Northwestern's MRSEC program (NSF DMR-1720139). We

This journal is © The Royal Society of Chemistry 2023

thank Applied Materials for supplying the trenched wafer used in this study.

Notes and references

1 B. Wang, W. Huang, L. Chi, M. Al-Hashimi, T. J. Marks and A. Facchetti, A. Chem. Rev. 2018, **118**, 5690-5754.
2 C. Wiemer, L. Lamagna and M. Fanciulli, Semicond. Sci. Technol. 2012, **27**, 074013.
3 J. Robertson, Eur. Phys. J. Appl. Phys. 2004, **28**, 265-291.
4 A. Ohtomo and H. Y. Hwang, Nature 2004, **427**, 423-426.
5 J. Mannhart, D. H. A. Blank, H. Y. Hwang, A. J. Millis and J. M. Triscone, MRS Bull. 2008, **33**, 1027-1034.
6 N. Reyren, S. Thiel, A. D. Caviglia, L. F. Kourkoutis, G. Hammerl, C. Richter, C. W. Schneider, T. Kopp, A. S. Ruetschi, D. Jaccard, M. Gabay, D. A. Muller, J.-M. Triscone and J. Mannhart, Science 2007, **317**, 1196-1199.
7 A. S. Patil, A. V. Patil, C. G. Dighavkar, V. A. Adole and U. J. Tupe, Chem. Phys. Lett. 2022, **796**, 139555.
8 M. E. Cruz, M. Sedano, Y. Castro, M. J. Pascual, J. Fernández, R. Balda and A. Durán, Opt. Mater. Express 2022, **12**, 3493-3516.
9 M. Losurdo, M. M. Giangregorio, G. Bruno, D. Yang, E. A. Irene, A. A. Suvorova and M. Saunders, Appl. Phys. Lett. 2007, **91**, 091914.
10 M. M. Giangregorio, M. Losurdo, A. Sacchetti, P. Capezzuto and G. Bruno, Thin Solid Films 2009, **517**, 2606-2610.
11 Y. Y. Zhu, R. Xu, S. Chen, Z. B. Fang, F. Xue, Y. Fan, X. J. Yang and Z. M. Jiang, Thin Solid Films 2006, **508**, 86-89.
12 V. Mikhelashvili, G. Eisenstein and F. Edelmann, Appl. Phys. Lett. 2002, **80**, 2156-2158.
13 H. Ono and T. Katsumata, Appl. Phys. Lett. 2001, 78, 1832-1834.
14 Y. Zhu, Z. Fang and Y. Liu, J. Rare Earths 2010, **28**, 752-755.
15 K. M. Hubbard and B. F. Espinoza, Thin Solid Films 2000, **366**, 175-180.
16 G. Scarel, A. Svane and M. Fanciulli, Scientific and Technological Issues Related to Rare Earth Oxides: An Introduction. In: M. Fanciulli and G. Scarel, (eds) Rare Earth Oxide Thin Films. Topics in Applied Physics, 2006, **106**. Springer, Berlin, Heidelberg.
17 V. A. Rozhkov and M. A. Rodionov, Tech. Phys. Lett. 2005, **31**, 77-78.
18 S. Chen, Y. Y. Zhu, R. Xu, Y. Q. Wu, X. J. Yang, Y. L. Fan, F. Lu, Z. M. Jiang and J. Zou, Appl. Phys. Lett. 2006, **88**, 222902.
19 L. Qiao, G. He, L. Hao, J. Lu, Q. Gao, M. Zhang and Z. Fang, IEEE Trans. Electron Devices 2021, **68**, 2899-2905.
20 X. Wang, Y. L. Zhu, M. He, H. B. Lu, and X. L. Ma, Acta Mater. 2011, **59**, 1644-1650.
21 Z. B. Fang, S. Chen, Y. Y. Zhu, Y. Q. Wu, Y. L. Fan, Y. Y. Wang and Z. M. Jiang, Nanotechnology 2007, **18**, 155205.
22 M. P. Hehlen, N. J. Cockroft, T. R. Gosnell and A. J. Bruce, Phys. Rev. B 1997, **56**, 9302-9318.
23 H. S. Kamineni, V. K. Kamineni, R. L. Moore, S. Gallis, A. C. Diebold, M. Huang and A. E. Kaloyeros, J. Appl. Phys. 2012, **111**, 013104.
24 X. Li, P. Wu, H. Qiu, S. Chen and B. Song, Thin Solid Films 2012, **520**, 2316-2320.
25 S. L. Morelhão, G. E. S. Brito and E. Abramof, J. Alloys Compd. 2002, **344**, 207-211.
26 F. Sánchez, X. Queralt, C. Ferrater, R. Aguiar and M. Varela, Vacuum 1994, **45**, 1129-1130.
27 G. L. M. Bonnet, J. C. Colson and J. P. Larpin, Thin Solid Films 1995, **261**, 31-36.
28 K. Xu, V.-S. Dang, A. Ney, T. D. L. Arcos and A. Devi, J. Nanosci. Nanotechnol. 2014, **14**, 5095-5102.
29 M. P. Singh, C. S. Thakur, K. Shalini, N. Bhat and S. A. Shivashankar, Appl. Phys. Lett. 2003, **83**, 2889-2891.
30 J. Päiväsaari, M. Putkonen, T. Sajavaara and L. Niinistö, J. Alloys Compd. 2004, **374**, 124-128.
31 A. Tamm, M. Heikkilä, M. Kemell, J. Kozlova, K. Kukli, V. Sammelselg, M. Ritala and M. Leskelä, Thin Solid Films 2010, **519**, 666-673.
32 T. T. Van, J. Hoang, R. Ostroumov, K. L. Wang, J. R. Bargar, J. Lu, H.-O. Blom and J. P. Chang, J. Appl. Phys. 2006, **100**, 073512.
33 J. Rönn, L. Karvonen, C. Kauppinen, A. P. Perros, N. Peyghambarian, H. Lipsanen, A. Säynätjoki and Z. Sun, ACS Photonics 2016, **3**, 2040-2048.
34 T. T. Van and J. P. Chang, Appl. Phys. Lett. 2005, **87**, 011907.
35 T. T. Van and J. P. Chang, Appl. Surf. Sci. 2005, **246**, 250-261.
36 M. Demirtaş and F. Ay, IEEE J. Selected Topics Quantum Electron. 2020, **26**, 3200208.
37 J. Päiväsaari, J. Niinistö, K. Arstila, K. Kukli, M. Putkonen and L. Niinistö, Chem. Vap. Deposition 2005, **11**, 415-419.
38 R. Xu and C. G. Takoudis, ECS J. Solid St. Sci. Technol. 2012, **6**, N107-N114.
39 T. Blanquart, M. Kaipio, J. Niinistö, M. Gavagnin, V. Longo, L. Blanquart, C. Lansalot, W. Noh, H. D. Wanzenböck, M. Ritala and M. Leskelä, Chem. Vap. Deposition 2014, **20**, 217-223.
40 I.-K. Oh, K. Kim, Z. Lee, K. Y. Ko, C.-W. Lee, S. J. Lee,J. M. Myung, C. Lansalot-Matras, W. Noh, C. Dussarat, H. Kim and H.-B.-R. Lee, Chem. Mater. 2015, **27**, 148-156.
41 P.-Y. Chen, A. B. Posadas, S. Kwon, Q. Wang, M. J. Kim, A. A. Demkov and J. G. Ekerdt, J. Appl. Phys. 2017, **122**, 215302.
42 P.-Y. Chen, T. Hadamek, S. Kwon, F. Al-Quaiti, A. B. Posadas, M. J. Kim, A. A. Demkov and J. G. Ekerdt, J. Vac. Sci. Technol. A 2020, **38**, 012403.
43 L. Khomenkova, H. Merabet, M.-P. Chauvat, C. Frilay, X. Portier, C. Labbe, P. Marie, J. Cardin, S. Boudin, J.-M. Rueff and F. Gourbilleau, Surf. Interfaces 2022, **34**, 102377.
44 R. Xu, Q. Tao, Y. Yang and C. G. Takoudis, Appl. Surf. Sci. 2012, **258**, 8514-8520.
45 M. Nolan and S. D. Elliott, Chem. Mater. 2010, **22**, 117-129.
46 J. Päiväsaari, C. L. Dezelah, D. Back, H. M. El-Kaderi, M. J. Heeg, M. Putkonen, L. Niinistö and C. H. Winter, J. Mater. Chem. 2005, **15**, 4224-4233.
47 K. Xu, A. R. Chaudhuri, H. Parala, D. Schwendt, T. D. L. Arcos, H. J. Osten and A. Devi, J. Mater. Chem. C 2013, **1**, 3939-3946.
48 A. Kurek, P. G. Gordon, S. Karle, A. Devi and S. T. Barry, Aust. J. Chem. 2014, **67**, 989-996.
49 S. M. George, Chem. Rev. 2010, **110**, 111-131.
50 M. Leskelä and M. Ritala, Angew. Chem. Int. Ed. 2003, **42**, 5548-5554.
51 T. P. Silverstein and S. T. Heller, J. Chem. Educ. 2017, **94**, 690-695.
52 J. March, Advanced Organic Chemistry, third edition, John Wiley & Sons, New York, 1985, pp. 220-222.
53 N. Jayakodiarachchi, P. G. Evans, C. L. Ward and C. H. Winter, Organometallics 2021, **40**, 1270-1283.
54 F. G. Bordwell, J. A. Harrelson, Jr. and T.-Y. Lynch, J. Org. Chem. 1990, **55**, 3337-3341.
55 Y. Chen, M. H. Yusuf, Y. Guan, R. B. Jacobson, M. Lagally, S. E. Babcock, T. F. Kuech and P. G. Evans, Appl. Mater. Interfaces 2017, **9**, 41034-41042.
56 M. Yoshimoto, T. Maeda, T. Ohnishi, H. Koinuma, O. Ishiyama, M. Shinohara, M. Kubo, R. Miura and A. Miyamoto, Appl. Phys. Lett. 1995, **67**, 2615-2617.
57 S. Jeon and H. Hwang, J. Appl. Phys. 2003, **93**, 6393-6395.
58 F.-H. Chen, J.-L. Her, Y.-H. Shao, Y. H. Matsuda and T.-M. Pan, Nanoscale Res. Lett. 2013, 8;8(1):18.